Advancing efficiency and reliability in thermal analysis of laser powder-bed fusion

Pooriya Gh Ghanbari [a,b], Rafal Wrobel [a,c], Bastian Rheingans [a], Thomas Mayer [d], Christian Leinenbach [a,e], Edoardo Mazza [a,b], Ehsan Hosseini [a,*]

[a] *Empa Swiss Federal Laboratories for Materials Science & Technology, Überlandstrasse 129, 8600 Dübendorf, Switzerland*
[b] *ETH Zürich, Department of Mechanical and Process Engineering, Institute for Mechanical Systems, Leonhardstrasse 21, 8092 Zürich, Switzerland*
[c] *ETH Zürich, Department of Materials, Laboratory for Nanometallurgy, Vladimir-Prelog-Weg 4, 8093 Zürich, Switzerland*
[d] *ZHAW School of Engineering, Institute of Mechanical Systems, Technikumstrasse 9, 8401 Winterthur, Switzerland*
[e] *École Polytechnique Fédérale de Lausanne (EPFL), Laboratory for Photonic Materials and Characterization, 1015 Lausanne, Switzerland*

ARTICLE INFO

ABSTRACT

In laser based powder-bed fusion of metals (PBF-LB/M), parts are fabricated by melting layers of powder using a high-intensity laser beam. During this process, the material is exposed to rapid cooling rates and intense thermal gradients, which are the underlying causes of residual stress formation and development of a unique microstructure in these components. Therefore, understanding the heat transfer phenomenon and reliably representing exposed temperature profiles in simulation frameworks are prerequisites for studying the microstructure and residual stress development during the PBF-LB/M process. This work employs a combination of experimental measurements and model development to study this phenomenon. Thermal properties of Hastelloy X were measured in the as-deposited state and used to setup finite element (FE) thermal simulations of the PBF-LB/M process. In addition, *in-situ* temperature evolutions near the laser tracks were measured by instrumenting thin-wall structures with K-type thermocouples in a two-stage fabrication process. The gathered data was used to calibrate uncertain modelling parameters, and ultimately, the simulation framework could closely represent the measured temperature histories. To address the high computational cost of FE thermal simulations, an adaptive-local/global multiscale modelling approach was proposed, which substantially reduced computation times without compromising the accuracy of the results. The modelling files and scripts are available in github.

1. Introduction

Metal additive manufacturing (MAM) has seen a surge of interest by industry in recent years owing to many advantages, including but not limited to high design freedom, near net-shape fabrication, and reduced end-to-end production times [1–3]. One of the most common MAM methods at the time of this writing is laser-based powder bed fusion of metals (PBF-LB/M), where powder layers are selectively consolidated by exposure to a high-intensity laser based on cross-section slices of a 3D model [2]. Even with the unique benefits, widespread adoption of MAM is still faced with issues regarding uncertainties in mechanical properties [4–6], and cracking or distortion due to thermal (residual) stresses [7–9]. To enhance the quality and integrity of the printed components, the build process and the link between process conditions and product properties need to be better understood [10]. This knowledge would allow for enhanced optimization of printing

parameters and realization of these new technologies to their maximum potential. However, due to involvement of many parameters in the fabrication process, optimization is a challenging task [10,11]. Experimental trial-and-error is often employed to find the best set of process parameters for each print job, which is extremely inefficient, expensive, and time-consuming [10,12–14], and hence an alternative should be sought.

Property differences of MAM components with respect to traditionally manufactured counterparts can be traced back to the thermal cycles exposed to the material during fabrication. Heating metal powder using a high-intensity laser beam creates a small melt-pool in the 100 μm length-scale [15,16], which leads to development of steep temperature gradients over 1×10^6 K/m in magnitude near the process zone. Combined with high scanning speeds in the range of 600 to 2000 mm/s [16], the material solidifies with cooling rates up to 1×10^6 K/s [17,18].

---

* Corresponding author.
E-mail address: ehsan.hosseini@empa.ch (E. Hosseini).

Rapid solidification in combination with repeated exposure to extreme temperature profiles results in a complex thermomechanical history. Consequently, a unique microstructure with a complex distribution of residual stresses develop within the part [15,19], and lead to material properties that differ from conventionally manufactured counterparts [20]. In particular, the residual stresses can cause problems such as cracking during the build process, or distortion after removing the component from the build-plate [8]. Studying these effects in depth requires a comprehensive knowledge of the temperature profiles and the thermal history during the build process.

Reaching this understanding through temperature measurements in PBF-LB/M is a challenging task due to the small scale and rapid transience of the process. One method involves using thermal cameras or pyrometers to monitor the radiations emitting from the uppermost layer [21–25]. For instance, Mohr et al. used an infrared camera to record temperatures in the 150 °C to 580 °C range [25]. To measure higher temperature levels, Hooper employed two cameras to cover the radiation in the visible light and near-infrared spectrum, which allowed temperature readings in the 1000 °C to 3000 °C range [24]. However, thermal cameras involve uncertainties due to variations in the emissivity of different surfaces over a wide range of temperatures and angles [21–23]. Another issue may arise from obstruction of the camera view by particle ejection or plume formation due to evaporation over the melt-pool, which introduces added uncertainties to these measurements [24,26].

Another approach uses thermocouples to measure the temperatures at a stationary location outside the melt-pool [1]. In many works, these sensors were placed on the build-plate to monitor the gradual temperature increase during the build process [27–31]. For instance, Dunbar et al. measured a peak temperature of 110 °C at the substrate, and compare the data with far-field temperature predictions of their simulations [27]. Similarly, Denlinger et al. placed these sensors on the build-plate and used the results to validate the thermal response of their thermomechanical models [28,29]. For enhancing the sensitivity of thermocouples for PBF-LB/M, Chiumenti et al. devised a setup to place the sensors on the fabricated part [32]. They interrupted the build process after fabricating a height of ≈2 cm, then removed the powder-bed, and placed the sensors inside holes on the vertical surface of the components. This allowed them to measure higher temperature peaks compared to previous works, and a similar approach was adopted for the fabrication process of thin-wall structures in this study. To facilitate higher fidelity temperature measurements in this study, we moved the sensors as close as possible to the laser tracks and directly welded them to the printed thin-walls. Furthermore, the exact locations of spot-welds were determined through SEM imaging to enable better interpretation of the gathered data.

While temperature measurements provide valuable insight into the thermal history of PBF-LB/M components, they are limited to the outermost surface, and too expensive for covering a wide range of processing conditions. Therefore, numerical methods such as the finite element (FE) approach are often used to complement them. Several studies [28,29,32–39], including the present work, adopted the continuum assumptions in combination with the FE analysis method to study heat transfer in the PBF-LB/M process. The main assumption in this approach involves treating all material states (including the powder layer and the liquid metal inside the melt-pool) as continuum media with equivalent properties. Even though the computational cost of such FE analyses is lower than higher fidelity models using computational fluid dynamics [40–42], the requirement of fine space and time discretization poses challenges for increasing the domain size [29].

Some researchers adopted the 'lumped heating' approach for reducing the computational cost of such simulations [32,43,44], where the sum of laser thermal energy over the duration of multiple tracks or layers is applied in one solution time increment. For example, Zah and Branner combined 20 powder layers into a single 1 mm 'meta-layer' to model the fabrication process of a double cantilever [43]. Chiumenti

et al. studied the effect of depositing the thermal energy on the scale of hatches, layers, and layer batches, which demonstrated a reduction of simulation times at the cost of reducing detailed representation of thermal cycles [32]. Importantly, this method cannot provide any information about large temperature gradients and fast cooling rates in the vicinity of the process zone, or explain the effect of adopting different scan patterns on the developed temperature field. Meanwhile, various studies have shown that variations in scan strategy, and its impact on temperature profiles, alter the characteristics of PBF-LB/M products [27,45–48]. For instance, Dunbar et al. and Song et al. showed that rotating the scan pattern between layers may lead to lower residual stress levels [27,47]. Parry et al. further investigated this link by studying the effect of scan vector length on variations in residual stress field distribution [45]. Therefore, there is a need for more efficient thermal simulations capable of accurately representing detailed temperature profiles.

Alternatively, various re-meshing techniques have been proposed to lower the computational cost of high-fidelity thermal simulations in PBF-LB/M by adaptively refining the mesh only around the moving heat source [30,49–53]. In some works, the mesh is only re-defined when a new layer is deposited. For example, Foteinopoulos et al. implemented such a technique for 2D thermal simulations [54]. Alternatively, Denlinger et al. used adaptive remeshing in their thermomechanical simulation framework to model the deposition process of a 6.3 mm × 6.3 mm × 2.3 mm cuboid [29]. These techniques have also been implemented for tetrahedral elements by Olleak and Xi [53]. Other works adaptively refined the mesh around the moving heat source during scanning process of a single layer [49,51,52]. However, this may increase the computational overhead for reconstruction of the stiffness matrix and transfer of solutions between dissimilar mesh distributions [30]. The optimal remeshing frequency requires numerical trial-and-error to best take advantage of the efficiency of these methods [52,53]. Alternatively, Luo and Zhao simply limited the refined region to one track at a time, and suggested that the computational advantages are sufficient [30].

Even though dynamic re-meshing optimizes the spatial discretization, small time steps are used to solve the temperature field for the entire modelling domain. Meanwhile, such fine incrementation is only needed in the process zone where the temperature evolution rates are high, whereas the far-field region can be solved with much larger time steps. Following this idea, our previous study proposed a 2D adaptive-local/global multiscale simulation strategy which applied the fine space and time discretization only around the melt-pool, and decreased computation times without compromising the reliability of the results [55]. The separation of scales allows for asynchronous time incrementation between the two models, and the proposed one-way global-to-local coupling facilitates parallel computation of the local simulations for further computational benefits. However, the 2D nature of the study did not allow for experimental validation of the performed analyses. Extension of the modelling strategy to 3D and comparisons with temperature measurements are the topics of the present study.

In the context of representativeness of such simulations, employment of reliable thermal properties over a large temperature range plays an important role. Acknowledging the documented differences in the microstructure of AM alloys versus their conventionally manufactured counterparts [56,57], the specific heat capacity and the thermal conductivity of additively manufactured Hastelloy X have been measured over a wide range of temperatures in this study and compared with literature data [58–60]. By employing the material data in the simulations, it could be shown that the developed FE model provides a good representation of the *in-situ* temperature measurements.

In the following, after describing the thermal characterization process of PBF-LB/M Hastelloy X, the developed setup for thermocouple-based temperature measurements during the build process is presented. Next, a detailed FE thermal model of the PBF-LB/M process is introduced and validated based on the *in-situ* measured temperatures. Lastly, the 3D adaptive-local/global multiscale simulation strategy and its reliability and computational gains are presented.

Table 1

Nominal composition of the Hastelloy X powder (average particle size of 30 μm) in wt-% (supplied by Oerlikon AM).

Ni	Cr	Fe	Mo	Co	W	C	Mn	Si	Cu	Al	Ti	P	S	B
Balance	21.7	18.6	9	1.5	0.6	0.06	<0.75	<0.75	<0.5	<0.5	<0.15	<0.02	<0.02	<0.01

Table 2

Process parameters used for PBF-LB/M of Hastelloy X samples.

Property	Value
Laser power (W)	125
Laser spot size d_{laser} (μm)	55
Powder layer thickness (μm)	30
Hatch distance (μm)	70
Scanning speed (mm/s)	700
Scanning strategy	Bidirectional

2. Characterization of thermal properties

During the MAM process, the material is exposed to a wide range of temperatures from the ambient level up to and above the melting point. In order to reliably represent the thermal response during fabrication, it is necessary to adopt a thermal material model that encompasses this wide range of temperatures. In the following, the procedures employed to measure the thermal conductivity and specific heat capacity of the alloy used in this study are described, and obtained results are compared with literature data.

Hastelloy X was chosen as the reference material in this study. This corrosion-resistant nickel-based superalloy has great tensile and creep performance at high temperatures, and is commonly used in PBF-LB/M to produce high performance components for applications such as gas turbines [20] and compact heat exchangers [61]. To measure the thermal properties of the as-deposited alloy, various samples were fabricated using commercially available gas-atomized Hastelloy X powder (chemical composition provided in Table 1) in a Sisma Mysint 100 (Sisma S.p.A., Italy) machine. A bidirectional scanning strategy with 90° rotation between layers was applied. The process parameters are reported in Table 2.

The thermal diffusivity of the alloy in the solid state was measured based on the laser flash analysis (LFA) technique using a Netzsch LFA 467 HT HyperFlash device. One side of a ⌀12.6 mm × 2.5 mm disk was exposed to a light pulse from a Xenon flash lamp (250 V, pulse width 600 μs) and the rise in temperature on the opposing side was measured by an InSb infrared detector (detected area diameter of 2.8 mm, measurement time of 2.5 s). The measurements took place under Ar atmosphere, with a heating rate of 5 K/min. At each temperature the thermal diffusivity was determined as an average of 5 shots. Between 20 °C and 450 °C a graphite coating was used to overcome the insufficient emissivity at lower temperatures. In the 450 °C to 1100 °C range, a sand-blasted surface was used to avoid unfavourable reactions with the graphite coating at elevated temperatures. The values of thermal diffusivity $D(T)$ were determined using an improved Cape-Lehman model [62,63] with pulse correction [64] that considers multi-dimensional heat loss and finite pulse widths.

Differential scanning calorimetry (DSC) was performed to determine the enthalpy change $\Delta H(T)$ of the alloy from room temperature to above the melting point using small disks with ⌀5.2 mm × 1 mm dimensions. The measurements were carried out on a Netzsch DSC 404 F1 high-temperature DSC apparatus at a constant heating rate of 20 K/min under Ar flowing atmosphere in the 30 °C to 1500 °C range. To mitigate the reaction between sample material and the crucible at elevated temperatures, PtRh20 crucibles with Al_2O_3 liner were employed. The heat flow as measured with DSC comprises the contribution of the specific heat capacity $c_p(T)$ of the material as well as any enthalpy change $\Delta H_{add}(T)$ caused by a material change upon heating, e.g., from phase transitions, precipitation reactions and melting.

$$\Delta H(T) = \int_{T_{ref}}^{T} c_p(\theta)\, d\theta + \sum_i \Delta H_{add,i}(T) \tag{1}$$

These effects can be combined by introduction of the effective specific heat capacity $c_{p,eff}$ such that:

$$\Delta H(T) = \int_{T_{ref}}^{T} c_{p,eff}(\theta)\, d\theta \tag{2}$$

The effective specific heat capacity below the melting point and the enthalpy of fusion were determined using the sapphire method (i.e. by conduction of reference measurements with sapphire disks) according to ASTM Standard E1269–11. Ultimately, the specific heat capacity, thermal diffusivity, and density were used to calculate the thermal conductivity of the material according to $k = D \times c_p \times \rho$ [62,63].

Fig. 1(a) compares the measured specific heat capacity with previous reports for Hastelloy X [58–60]. The results show an exothermic effect in the 430 °C to 620 °C range, similar to an observation by Kim et al. [65] for Alloy 600, which was attributed to an order–disorder transformation that strongly depends on the thermo-mechanical history of the material. They have reported this phenomenon for water quenched samples while slow furnace cooling after solution heat-treatment caused the exothermic effect to disappear. In this context, the discrepancy between the DSC measurements of the current study and those provided by Ulan et al. [60] may be explained by the different thermo-mechanical histories. The samples of the present study were produced by PBF-LB/M and thus experienced faster cooling-rates than the samples investigated in [60] which were heat-treated and subsequently air-quenched. In Fig. 1(b) the calculated thermal conductivity is compared with literature data [58–60]. The thermal diffusivity D was observed to continuously increase with temperature up to 700 °C, but a change in the slope of the thermal conductivity k was observed between 400 °C and 600 °C. This effect is caused by the direct proportionality of k to c_p and the previously mentioned exothermic reactions in the DSC measurements.

3. *in-situ* temperature measurements in PBF of thin-wall samples

To calibrate uncertain modelling parameters and validate the predictive capability of PBF-LB/M thermal simulations, it is crucial to gather experimental data on the evolving temperature distribution throughout the process. In this study, *in-situ* measurements using spot-welded thermocouples were employed to obtain this information. The experimental campaign dedicated to temperature measurements close to laser tracks in PBF-LB/M of HX thin-wall structures and the results obtained are discussed next.

Two thin-walls corresponding to 2 and 3 laser tracks in thickness (denoted by sample T2 and sample T3, respectively) were printed up to an initial height of 6 mm using the process parameters provided in Table 2. To allow for sensor installation, the build-plate was taken out of the printing machine and two K-type thermocouple pairs were spot-welded near the top and at the bottom of each thin-wall. The build-plate was placed back in the machine and an additional height of 2 mm was printed on top. During this stage, the signals from the thermocouples were recorded at a frequency of 9.6 kHz using a QuantumX MX840B amplifier. Information about the estimated time-response of the sensors is provided in Appendix A. A schematic of the setup and thermocouple placement configuration for sample T2 are shown in Fig. 2.

The placement of thermocouples close to the laser tracks allowed for measurement of higher temperature peaks and cooling rates compared to those from [32] (see Fig. 2(c)). Through subsequent scanning electron microscopy (SEM), the distance of thermocouple welds from the first print interface were measured to be 150 μm and 500 μm for
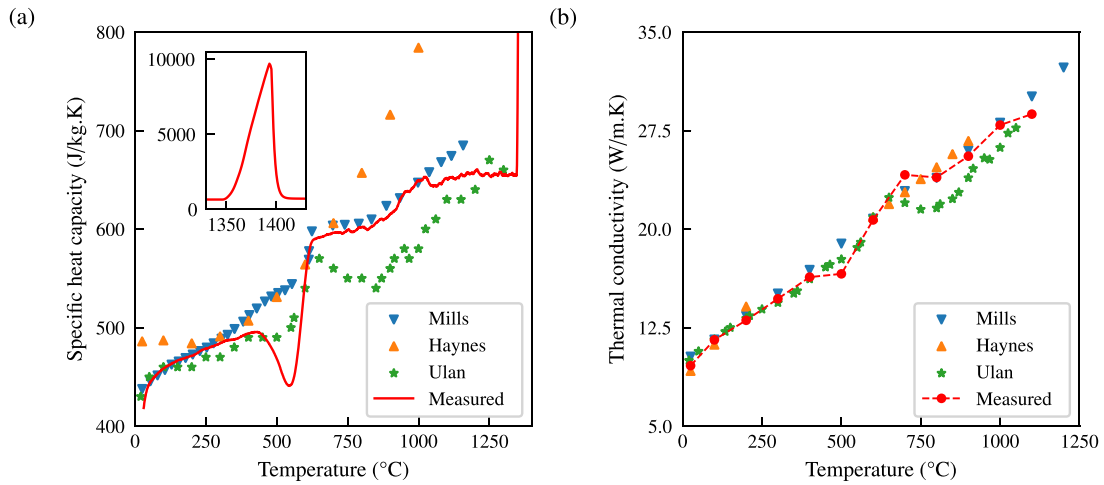
(a)

(b)

Fig. 1. Comparison of thermal properties of Hastelloy X samples, fabricated by PBF-LB, with reported values by Mills et al. [58], Haynes [59], and Ulan et al. [60]. (a) Effective specific heat capacity with an inset showing the effect of latent heat of fusion in the solidus (1357.6 °C)–liquidus (1399.5 °C) temperature range. (b) Thermal conductivity.
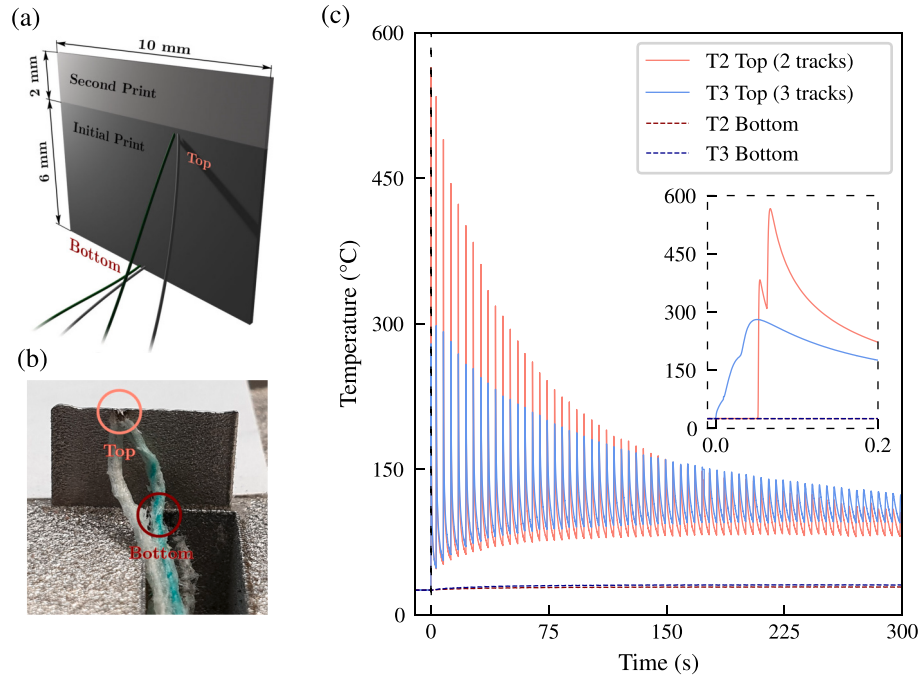

Fig. 2. Overview of the setup and results obtained in the *in-situ* temperature measurement campaign. (a) Schematic of the geometrical dimensions used in the first and second stage of printing. (b) A photo of sample T2 after attachment of thermocouples, before the second fabrication step. (c) Measured temperatures near the laser tracks (top) and the base of the structures (bottom). The inset focuses on the first layer. The lower temperature peaks in sample T3 are attributed to farther placement of the thermocouples from the laser tracks (500 μm versus 150 μm). However, the cooling curves between layer depositions are at a higher temperature level for T3 due to 50% nominal increase in deposited thermal energy.

samples T2 and T3, respectively. The smaller sensor distance from the laser tracks in T2 explains the higher measured temperature peaks for this sample in Fig. 2(c). Towards the end of the measurements, sample T3 reaches higher temperature levels due to greater heat accumulation from scanning of 3 tracks instead of 2 per layer. These measurements were used to assess the validity of the FE modelling framework in the following section.

4. Finite element thermal modelling of PBF-LB/M

Although temperature measurements offer valuable information about the evolving temperatures during the PBF-LB/M fabrication process, they are time-consuming to perform and constrained to a single spot per sensor. To overcome these limitations, FE thermal analysis can

be employed to simulate the PBF-LB/M process using the measured properties described in Section 2, and calibrated based on *in-situ* temperature measurements of Section 3. The modelling assumptions and general setup of the developed FE thermal simulation framework are outlined next, followed by a discussion on the calibration process of the uncertain parameters.

Two models corresponding to samples T2 and T3 were created to represent the observed temperature histories during the measurements described in the previous section. To this end, the commercially available FE software package Abaqus was used. The thermal energy conservation law in continuum-based thermal modelling can be written in the differential form as [55]:
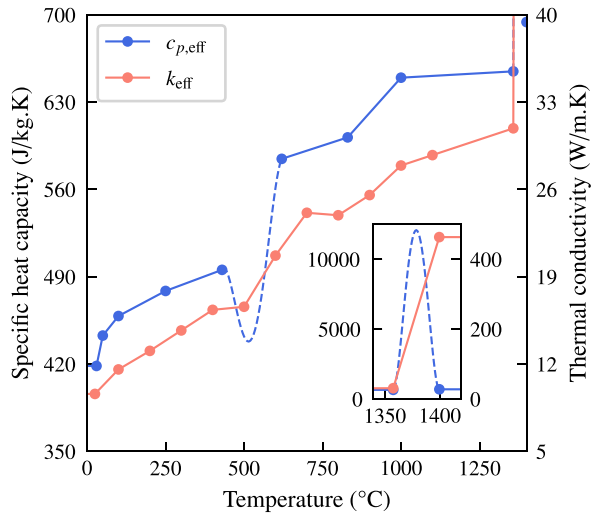
$$\rho c_p \dot{T} - \nabla \cdot (k \nabla T) = q_{\text{vol}} \qquad (3)$$

Fig. 3. The effective specific heat capacity $c_{p,\text{eff}}$ and thermal conductivity k_{eff} of Hastelloy X, that were adopted based on measurement data for application in the thermal simulations. The inset focuses on the solidus–liquidus temperature range.

Fig. 4. Schematic of the general Goldak double ellipsoid heat source model.

where temperature T is the time- and space-dependant variable, and the volumetric heat generation term q_{vol} represents the contribution of the moving heat source. The material properties ρ, c_p, and k are the density, specific heat capacity, and thermal conductivity, respectively. The temperature dependence of these parameters was defined based on the outcome of the measurements in Section 2, with modifications that are explained in the following.

The density ρ was assumed to be constant and equal to the measured value at room temperature 8352 kg/m^3 $\pm$2% similar to [30,66]. Correspondingly, the model geometry was configured based on measured dimensions at room temperature. The temperature dependence of the specific heat capacity c_p in the 30 °C to 1500 °C range was determined based on the DSC measurements. The measured enthalpy of fusion of 225 kJ/kg was implemented using the *apparent capacity* method [67] via a bi-quadratic increase in the effective specific heat capacity $c_{p,\text{eff}}$ over the solidus–liquidus range (i.e. Eq. (2)) similar to [33]. This effect is denoted by dashed lines in Fig. 3. In order to reduce the non-linearity of the material model and consequently decrease simulation times, the solidus-liquidus temperature range was increased ($\Delta T_{\text{solidification}} = 400$ °C) wherever the accuracy of the results in the point of interest was assured. While this simplification affects the simulations results in the process zone, the far-field temperatures remain unchanged as shown in Appendix B. Similarly, the exothermic effect observed around 500 °C was applied as an equivalent decrease of 10.08 kJ/kg in $c_{p,\text{eff}}$ over the temperature range of 430 °C to 620 °C.

The thermal conductivity k was implemented with temperature-dependence based on measurements of Section 2 in the 25 °C to 1100 °C range as shown in Fig. 3. The conductivity at the solidus temperature was linearly extrapolated from the data. For the liquid material inside the melt-pool, convection by mechanisms such as Marangoni and buoyancy enhances the distribution of thermal energy and contributes towards temperature homogenization. In order to compensate for the lack of fluid flow consideration and the resulting convective heat transfer in the models, the thermal conductivity of the alloy above the melting point may be artificially increased with respect to the value at the solidus temperature [30,68]. Following [30], a factor of ×15 was chosen in this study.

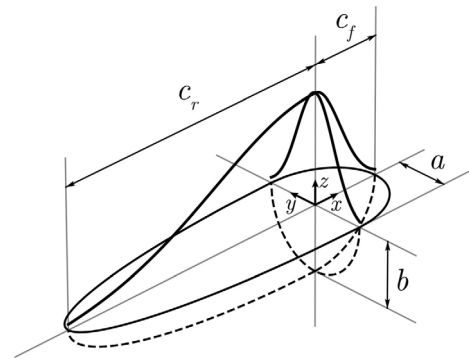The volumetric heat generation term q_{vol} in Eq. (3) was assigned using the Goldak heat source model [68] following previous works [13,34,47] which can be represented in the general form as:

$$q_{vol} = \eta \frac{6\sqrt{3}f_{f/r}P}{abc\pi\sqrt{\pi}}\exp\left(-\frac{3x^2}{c_{f/r}^2}\right)\exp\left(-\frac{3y^2}{a^2}\right)\exp\left(-\frac{3z^2}{b^2}\right) \tag{4}$$

where x, y, and z are the spatial coordinates in a moving Cartesian system attached to the centre of the laser spot (see Fig. 4), η is the laser absorption coefficient, P is the laser power, and f_f and f_r are fractions of laser energy that are, respectively, absorbed in the front and rear half of the ellipsoid, such that $f_f + f_r = 2$. The parameters a, b, and c are the principle radii of the ellipsoid as shown in Fig. 4, and are commonly calibrated based on measured melt-pool dimensions [37,38]. Since the melt-pool size could not be consistently measured for the printed thin-walls in this study, the ellipsoid was simplified to a circle with $a = c_{f/r} = d_{\text{laser}}/2$ similar to [31,39,47], and b was chosen equal to the powder layer thickness [39].

The heat transfer problem was resolved with the Abaqus/standard solver. Based on a mesh sensitivity analysis provided in Appendix B, hexahedral 8-node linear brick elements (DC3D8) with dimensions in the 20 μm to 100 μm range were used. Time increment size was primarily determined using the automatic incrementation algorithm of Abaqus/standard based on the default convergence settings, notably a maximum allowed residual heat flux of 0.5% and a 1% limit on nodal temperature corrections. In order to take advantage of the lower sensitivity of far-field temperatures to the discretization level (Appendix B), the mesh was configured such that smaller elements were applied only around the region probed by the thermocouples. Further measures were taken to ensure that the solver uses smaller time increments when the laser is near the probed regions, while larger increments were allowed otherwise. More details of the *adaptive time incrementation* method are discussed in Appendix C. Henceforth, models with these considerations are referred to as *probe* simulations. It should be noted that the reliability of the resulting temperature history is limited only to the region of interest. Nevertheless, in the case of calibrating modelling parameters based on thermocouple data, this approach provided the necessary information at a lower computational cost.

Corresponding to Fig. 2(a), the T2/T3 samples were modelled as $10 \times 6 \times 0.17/0.22$ mm^3 assemblies, where the wall thicknesses were determined based on SEM imaging. The built-in subroutines of the Abaqus AM modeller plug-in were used to implement the moving heat source, which were previously verified in [33]. The plug-in was also used to implement 10 layer depositions based on the *quiet element* method, where the elements of inactive layers do not contribute to the calculations until activated by movement of the recoater.

The simulations started with initial room temperature (25 °C) over the whole domain. The *in-situ* readouts from the bottom thermocouples were assigned to the bottom surface of the structures as boundary
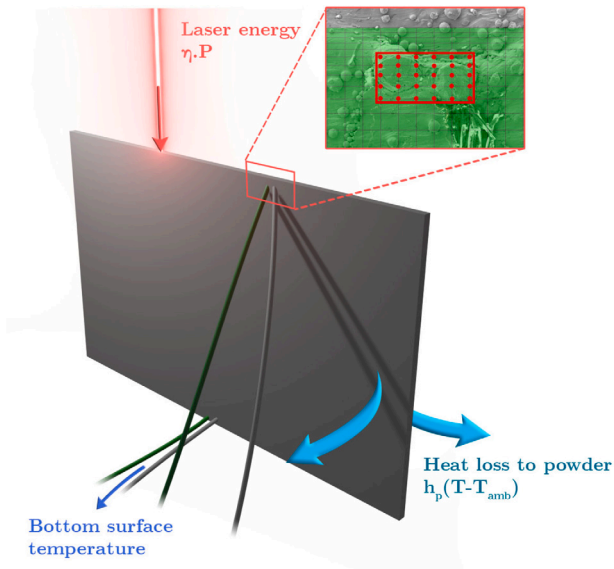
Fig. 5. Schematic of the thin-wall geometry used to setup the FE model and its boundary conditions, namely, the thermal load from the laser heat source, heat loss to the powder bed based on Newton's law of cooling, and bottom surface temperatures assigned based on bottom thermocouple readings. The precise spot-weld location was determined via SEM imaging, and an average over encompassing nodes was used to compare simulation predictions with measurement data.

conditions. To reduce the computational efforts, properties for the top-most deposited powder layer were considered similar to solid material, as it is shown in Appendix B that such an approximation has little influence on temperatures in the region of interest. Heat loss to the powder-bed q_p was implemented based on Newton's law of cooling as an equivalent convective heat loss h_p over all model surfaces ($q_p = h_p(T - T_{amb})$, where $T_{amb} = 25\ °C$) similar to [29,30,69]. Li et al. [69] showed that h_p varies with the thickness of the printed geometry, and is expected to be over $20\ \mathrm{W\,m^{-2}\,K^{-1}}$ for the $\approx 0.2\ \mathrm{mm}$ thin-walls. The second unknown and difficult to measure parameter was the laser absorption coefficient η which can vary in a wide range (30%–70% for single-track PBF-LB/M of Hastelloy X [70]) for different process parameters [70,71]. In this study, the experimental measurements from sample T2 were used for calibrating η and h_p, while sample T3 was used as an independent benchmark. Fig. 5 presents an overview of the developed modelling setup. *Probed* regions were defined as the locations of top thermocouple attachments in the conducted experiment (Fig. 5(b)). The corresponding nodal temperature history over these areas were averaged and compared with the experimental readouts.

A search in the parameter space for η and h_p leads to 48% for the absorption coefficient and $25\ \mathrm{W\,m^{-2}\,K^{-1}}$ for the equivalent convective heat loss to the powder-bed for reaching a good match with thermocouple data. Fig. 6(a) shows the temperature histories for sample T2 based on measurements and simulations with three different sets of η and h_p. More combinations of η and h_p values are provided in Appendix D, where the sensitivity of calculated temperature histories to these two parameters is demonstrated. While η affected both the temperature peaks and the cooling behaviour, the changes in peak values with h_p were small. Nevertheless, noticeable variations in the cooling portion of the curves for different h_p were observed, which enabled fine-tuning these parameters.

Regardless of the chosen value for h_p, heat accumulation in the samples was under-predicted by the models. That is to say, the simulations overestimated the cooled-down temperature at the end of first layer deposition, while underestimating this quantity for higher layers.
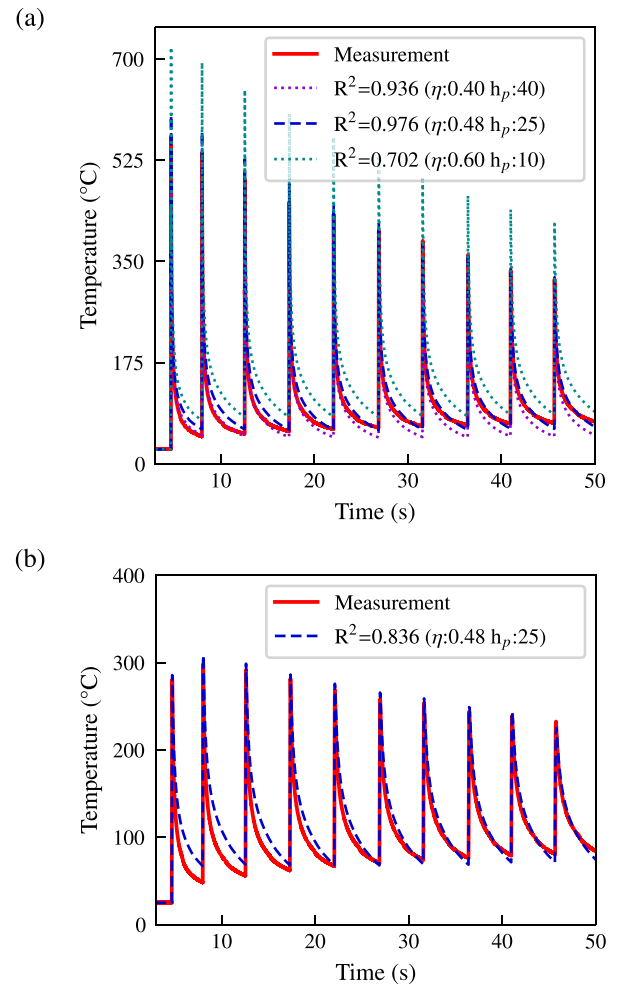

Fig. 6. Comparison of FE-predicted temperature histories with measurements. (a) Sample T2 thermocouple data was used to tune the uncertain parameters η and h_p. The effect of changing these parameters is shown in the dotted curves for two additional combinations. More examples are provided in Appendix D. (b) Comparison of the measured temperature history on sample T3 with respective model predictions using previously calibrated parameters.

This mismatch might originate from the simplification of conductive heat loss to powder as simple equivalent convection, which could be resolved by a more robust model via assuming temperature-dependent $h_p(T)$ similar to [72] or directly including powder elements around the thin-walls.

As an independent benchmark, the calibrated model was used to compare the simulation results with the experimental observations in sample T3 as shown in Fig. 6(b). Generally, a good agreement can be observed which demonstrates the effectiveness of the developed modelling framework. However, the lower coefficient of determination indicates that a change in the geometry leads to variations in heat transfer conditions and consequently the temperature histories. Therefore, the calibrated parameters are most representative of thin-wall structures, and their extension to other geometries may be limited.

In terms of computational costs, using 12 threads of an Intel Xeon processor, the simulation times for samples T2 and T3 were 6.1 and 10.4 h, respectively. The adaptive time incrementation approach outlined in Appendix C keeps the computational costs relatively low for the present case-study, but often the temperature profiles over the whole simulation domain is needed to perform, e.g., mechanical or microstructural analyses. The high computational cost of general-purpose

FE thermal analysis of PBF-LB/M, particularly for larger simulation domains, calls for a more efficient modelling approach. The following section proposes a multiscale simulation strategy and discusses the effectiveness of the method in providing the required thermal information at a much lower computational cost.

5. Multiscale approach

FE thermal simulations can offer a comprehensive overview of the temperature evolution within a component during the manufacturing process. However, their high computational cost limits their practical usage, particularly in applications such as parameter sensitivity studies, or sequentially coupled modelling frameworks involving microstructural analysis and thermomechanical simulations. In such cases, a faster and more efficient thermal model is necessary. A mesh sensitivity analysis (described in Appendix B) reveals that the temperature profiles converge more quickly in the far-filed with mesh refinement, compared to the process zone. In the following, a multiscale modelling framework is introduced that leverages this attribute. A two-part adaptive-local/global simulation framework is proposed to decrease computational costs while maintaining numerical accuracy.

Since steep temperature gradients and fast cooling rates in PBF-LB/M move with the laser-illuminated region, application of fine space and time discretization in FE thermal modelling is necessary only at the local vicinity of the process zone [55,73]. Therefore, a low-cost *global* model with coarse discretization can calculate the temperature profiles with adequate accuracy away from the laser interaction area (i.e., the far-field region) as demonstrated in Appendix B. To compensate for the loss of detail in the process zone, small-scale *local* simulations with fine mesh and small time increments can be used to recalculate the temperature values in the affected region. Eventually, combining the global simulation results with the local corrections represents the temperature history of an PBF-LB/M part at a significantly lower computational cost. It is important to note that the accuracy of the far-field temperature field in the global model does not depend on local simulations, which eliminates the need for a complex two-way coupling link between the two models. Furthermore, the one-way coupling allows for parallel calculation of local models for different tracks/layers to make better use of computational resources.

A schematic overview of the coupling between the two scales is shown in Fig. 7. First, the global model is solved with coarse discretization which provides reliable far-field temperatures that would be used as boundary conditions in the local simulations. Then, a python script is used to determine the activation time and spatial position of local models based on the laser scan path. For each laser track, the initial temperatures in the first local model are determined based on the global results (Fig. 7(a)). In the next local models, the initial temperatures are imported from the previous local model solution in the overlapping region and the global model otherwise (Δx_{local} in Fig. 7(b)).

For numerical verification, the proposed approach was compared with a reference model based on 3 layer depositions of sample T3 described in Section 4. To have reliable results for the whole domain, the measures used in probe simulations discussed in Appendix C could not be used, and uniform fine discretization with 10^3 μm³ elements and ≈4 μs time increments were applied in the reference simulation. This change led to a steep increase in computational costs, which made this simulation too expensive (estimated to take over 500 h), and thus necessitated a simplification involving neglecting the temperature-dependence of the material properties. The constant material properties were consistently used for both the reference and multiscale models. In the multiscale framework, the global model used average time increments of 20 μs and brick elements with minimum ≈22 μm × 50 μm × 30 μm size based on a mesh sensitivity analysis similar to Appendix B. The element size in the global model was further constrained by the laser-spot radius along its width, and the powder layer thickness for the vertical dimension. On the other hand, the local models used 10^3
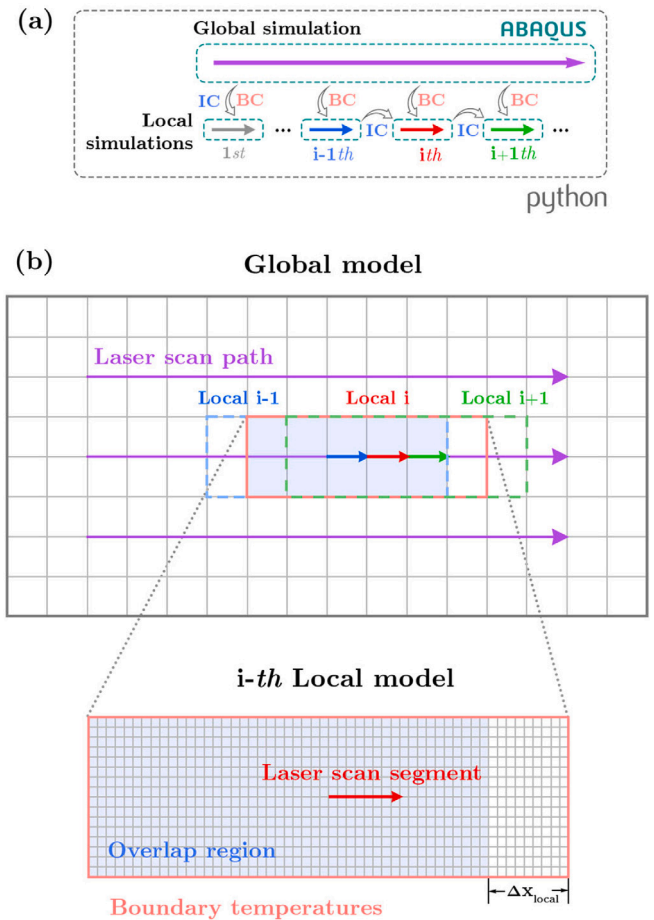

Fig. 7. Overview of the adaptive-local/global multiscale modelling framework. (a) Python scripts were used to run the global simulation, define the sequence of local models, and run the local simulations using the Abaqus solver (IC: Initial conditions, BC: Boundary conditions). (b) Schematic representation of the coupling between local–global simulations. The local models follow the heat source and re-calculate the temperature profiles in the process zone using boundary conditions based on the global results.

μm³ elements similar to the reference setup, with a 0.32 mm × 1.4 mm × 0.3 mm domain size around the laser.

With above considerations, the reference calculation lasted 151.4 h on an 18-core Intel Xeon Gold 6150 processor using a Linux-based installation of Abaqus 2021. On the other hand, the global simulation of the multiscale approach took only 1.2 h using the same computational resources. To use the multi-core processor efficiently, the local models were divided into 9 batches (corresponding to the laser tracks) and were solved in parallel. With this approach, all 900 local simulation were finished after 2.6 h. Overall, the proposed strategy decreased the computational time by a factor of 40. An even higher computational cost reduction is expected for larger simulation domains. Table 3 provides more details about the simulation parameters.

Fig. 8 compares the calculated temperature profiles from the two approaches at the start, middle and end of the process. The maximum observed error in the multiscale approach was 11 °C which is negligible in comparison with the calculated temperature values in the range of 25 °C to ca. 2800 °C. Therefore, the developed multiscale simulation strategy provides excellent accuracy with respect to the conventional modelling approach while significantly cutting back on computation times.
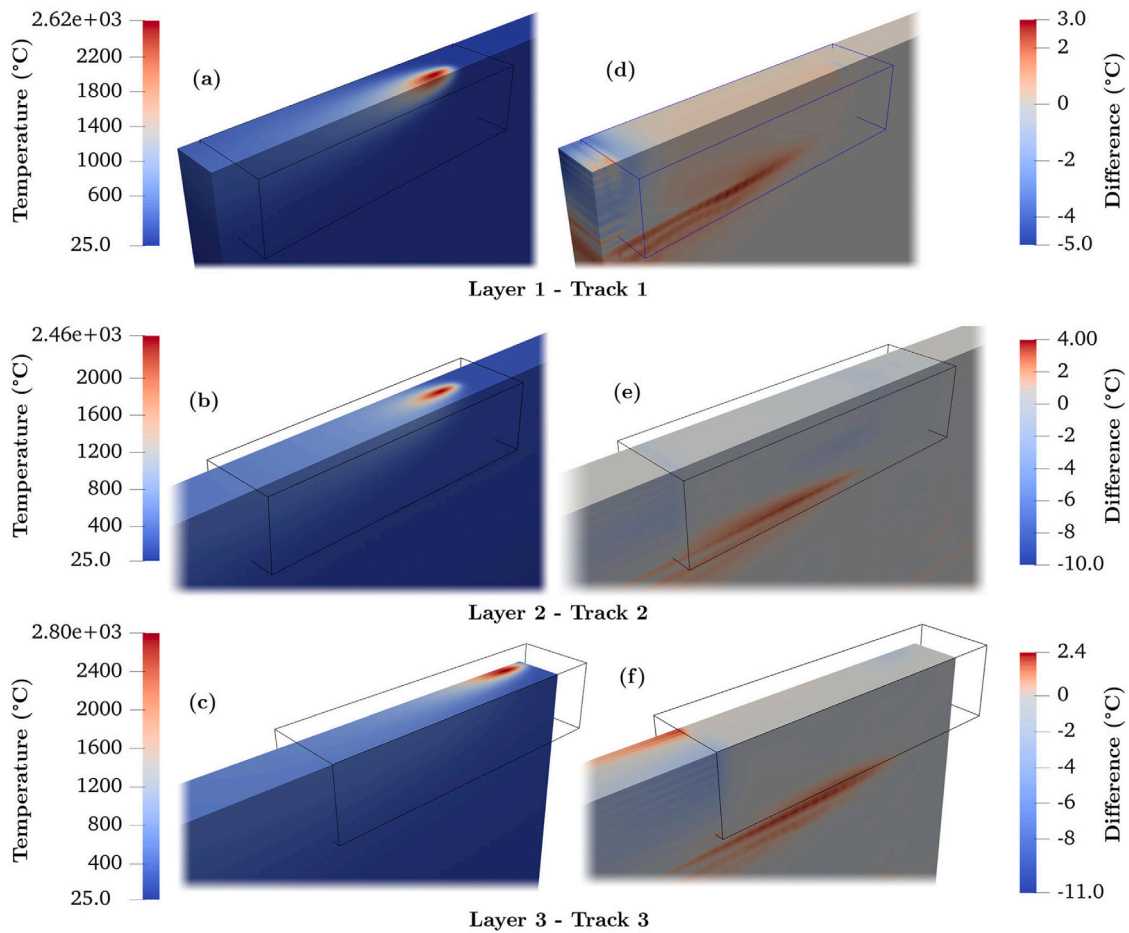
Fig. 8. Comparison of the combined local–global temperature distributions with a reference FE model employing fine discretization over the entire laser-scanned region. (a,b,c) The multiscale temperature profiles in the beginning of layer 1, middle of layer 2, and towards the end of the layer 3, respectively. (d,e,f) The difference $T_{\text{multiscale}} - T_{\text{reference}}$ between the two solutions outlined in figures a, b, and c.

Table 3
Model parameters used for numerical verification of the multiscale approach.

Property	Value
Laser power (W)	125
Absorption coefficient η (%)	50
Powder layer thickness (μm)	30
Hatch distance (μm)	70
Scanning speed (mm s^{-1})	700
Scanning strategy	Unidirectional
Material properties	
Thermal conductivity (W m^{-1} K^{-1})	50
Specific heat capacity (J kg^{-1} K^{-1})	486
Density (kg m^{-3})	8220
Goldak parameters	
a (μm)	40
b (μm)	60
c_f (μm)	60
c_r (μm)	240
f_f (–)	0.4
f_r (–)	1.6

To show the versatility of the multiscale method, it was adopted for modelling the 10-layer deposition process of sample T3 with consideration of temperature-dependent material properties introduced in Section 4. Additionally, the measured solidus-liquidus range of 42 °C was used in the local models to ensure the reliability of temperature predictions in the process zone. Fig. 9 compares the predicted temperature profiles from the multiscale simulation at the thermocouple location in sample T3 with calculations of Section 4 and the experimental measurements. The multiscale approach shows the same temperature history as probe simulations with similar experimental relevance. It is worth mentioning that combining such level of detail with uniform fine discretization over the whole domain would result in extremely long simulation times upwards of hundreds of hours. Even with the laser-adaptive time incrementation measures described in Appendix C, the probe simulation took 10.4 h to provide a reliable temperature history over a small limited volume, while the multiscale approach resolved the entire domain in about half the time at 5.6 h. Table 4 provides an overview of the adopted discretization and computational cost of the models.

Overall, the two series of simulations performed in this section emphasize the large impact of discretization on the computational cost of FE thermal analysis in PBF-LB/M. In both cases, the adaptive-local/global approach significantly reduced simulation times without compromising the accuracy of the results. For accessibility, the scripts and input files used for this study are readily available under https://github.com/HighTempIntegrity/Ghanbari_Multiscale2023. It should be noted that in verification of the multiscale approach, a simple unidirectional scanning strategy was examined. Further development is required for modelling complex scanning strategies to enhance transfer

Table 4

Overview of the discretization level and computational costs of models used in verification and validation of the multiscale approach.

Model	Element[a] (mm^3)	Increment[b] (µs)	Run time (h)
Verification with constant properties for 3 layers			
Reference	$10 \times 10 \times 10$	2 to 6	151.4
Locals	$10 \times 10 \times 10$	2 to 6	2.6
Global	$22 \times 50 \times 30$	20	1.2
Validation with temperature-dependent properties for 10 layers			
Probe	$20 \times 50 \times 30$	50 to 1000	10.4
Locals	$10 \times 50 \times 30$	1 to 10	5.0
Global	$36 \times 100 \times 30$	80 to 1400	0.6

[a]The average size of brick elements in the heated region in terms of width (hatch direction) × length (scan direction) × height (build direction).

[b]The approximate range of time increments for when the laser heat source is active.
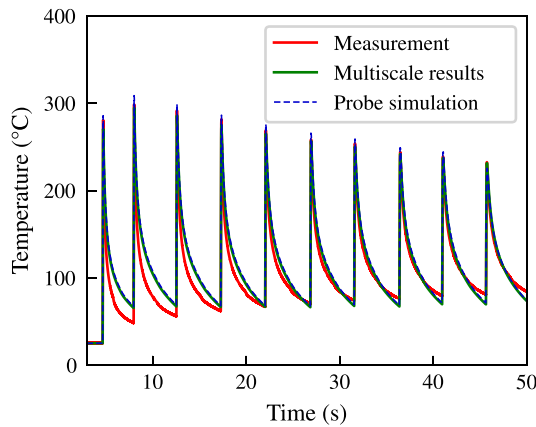

Fig. 9. Comparison of temperature profiles predicted with the multiscale approach at the thermocouple location in sample T3 with experimental measurements and the outcome of probe simulation, indicating the reliability of the multiscale method.

of information between global and local models and among consecutive locals models.

It is worth mentioning that the local models form a series of well-defined thermal problems that share the same mesh and time-span but differ only in their initial and boundary conditions. Based on this work, it might be possible to define a numerical surrogate for the local models that is trained based on a limited sample set, as demonstrate for 2D in [74]. By replacing the local FE models with the computationally cheap numerical surrogate, computational costs of the multiscale modelling strategy would be further reduced. This improvement would allow for thermal analysis of larger PBF-LB/M parts, with the ultimate goal of high-fidelity simulations at the component-scale.

6. Concluding remarks

Reliable and efficient heat transfer models are an integral component of sequentially coupled simulation frameworks for MAM processes. This study explored this topic through a combination of experiments and numerical model development. An overview of obtained results is provided in the following.

To create reliable thermal simulations for the PBF-LB/M process, and minimize uncertainties stemming from differences in the physical properties between PBF alloys and conventionally manufactured counterparts, the specific heat capacity and thermal conductivity of as-deposited Hastelloy X were directly characterized. While the thermal conductivity values showed little difference with respect to literature
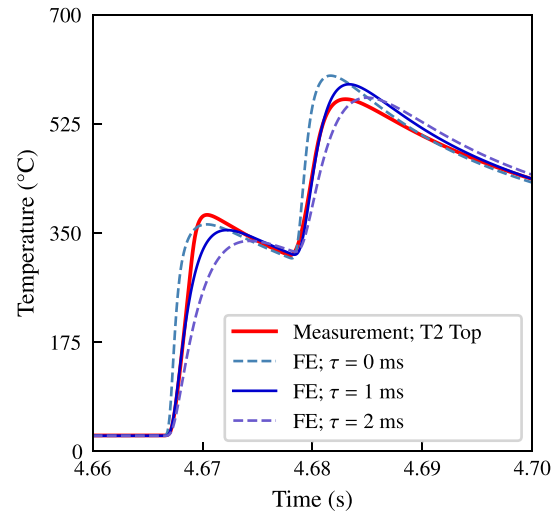

Fig. A.1. Effect of thermocouple response lag using different time-constants on simulated temperature histories. $\tau = 1$ ms results in the closest match between the model predictions and measurements.

data, a rare exothermic effect was observed in the 430 °C to 620 °C temperature range in differential scanning calorimetry of this alloy.

Furthermore, it was essential to gather *in-situ* information about the temperature histories occurring during the printing process to calibrate uncertain modelling parameters, and assess the validity of simulation predictions. To reach this objective, an experimental campaign was designed to measure the temperature history close to laser tracks during the fabrication of thin-wall structures. The printing process was interrupted to remove the samples from the build chamber and spot-weld K-type thermocouples to the thin-walls. Then, the instrumented samples were placed back in the printing machine, where temperature peaks up to 560 °C during multiple layer depositions were measured with a high temporal resolution (104 µs).

Representative models of the experiments were created in the Abaqus FE software package. Special measures were adopted to reduce the computational costs by limiting the model accuracy to the region probed by the thermocouple. To achieve this, an adaptive time incrementation routine was implemented in Abaqus, which sped-up simulations for calibrating two unknown modelling parameters, namely the laser absorption coefficient and an equivalent powder-bed heat loss coefficient. Once calibrated, the model could closely match the measured temperature history during laser scanning of the 2-track thin-wall structure. Validation based on the recorded thermal history on the 3-track thin-wall showed good accuracy with only a marginal increase in errors.

In the last part of this work, the setup and verification of a multiscale modelling approach for reducing the computational cost of thermal FE simulations were presented. It was shown that the far-field temperature histories can be well represented by relatively coarse decortication in a global model. For process zone temperatures, local simulations with fine discretization were created that imported the far-field global results as boundary conditions, and re-calculated the high-gradient temperature profiles. Thus, instead of solving a single finely discretized simulation, the proposed method used one low-cost global model, and a series of small-scale local simulations. Comparisons with a reference FE simulation with uniform fine discretization showed that the numerical accuracy of the temperature field could be preserved, while the simulation times were reduced by a factor of 40. In summary, separation of scales to adaptive-local and global
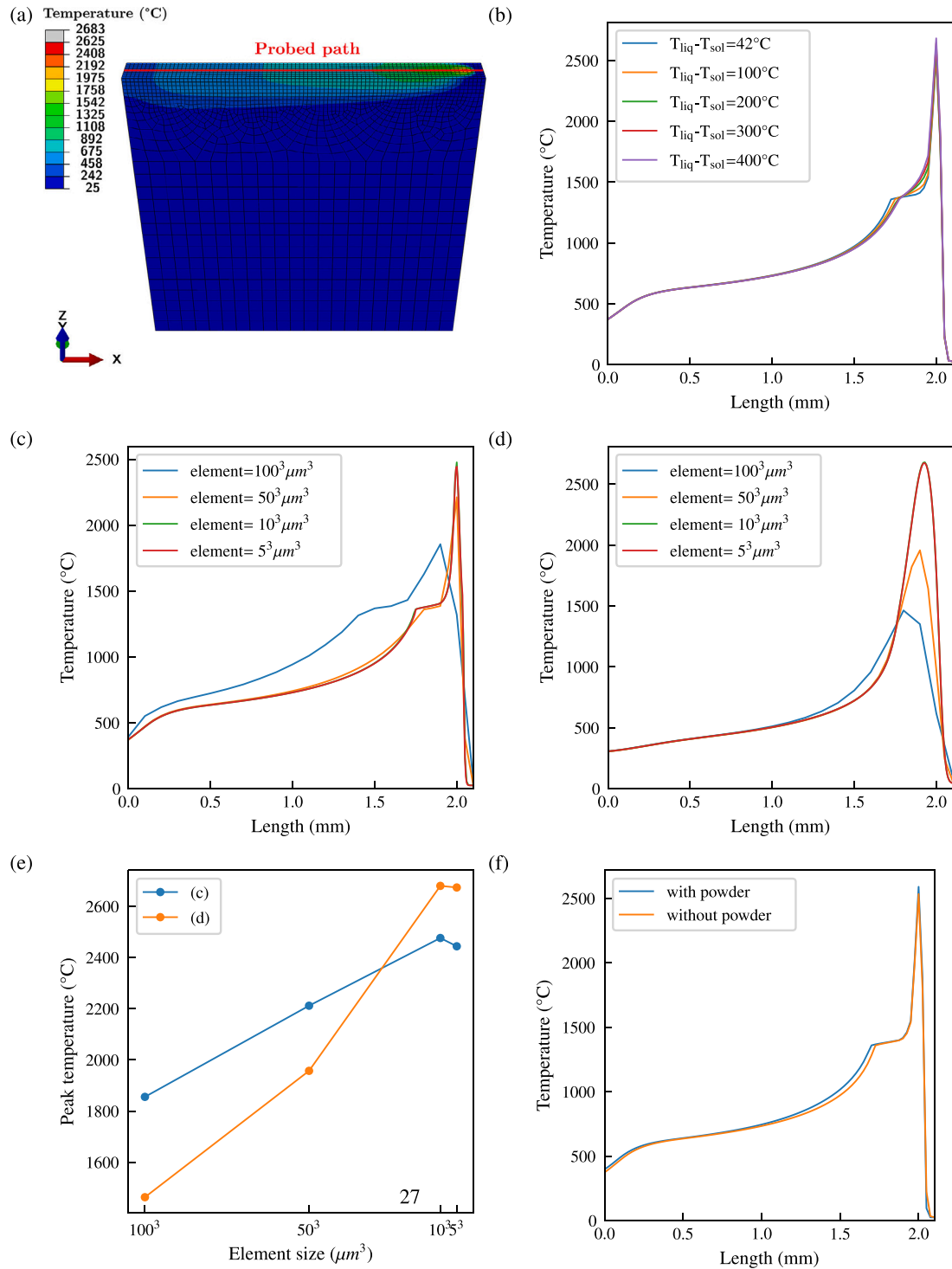
Fig. B.1. Sensitivity of simulated temperature distributions to various modelling assumptions. (a) The example geometry used to run the sensitivity analysis. Temperature distributions are plotted over the probed path at the end of laser-scanning a 2 mm track. (b) Variations in the solidification range. (c) Variations in element size with material properties outlined in Fig. 3. (d) Variations in element size with material properties outlined in Table 3. (e) Convergence of peak temperature value with refined mesh size in figures c and d. (f) Effect of reduced heat conduction to deposited powder layer.
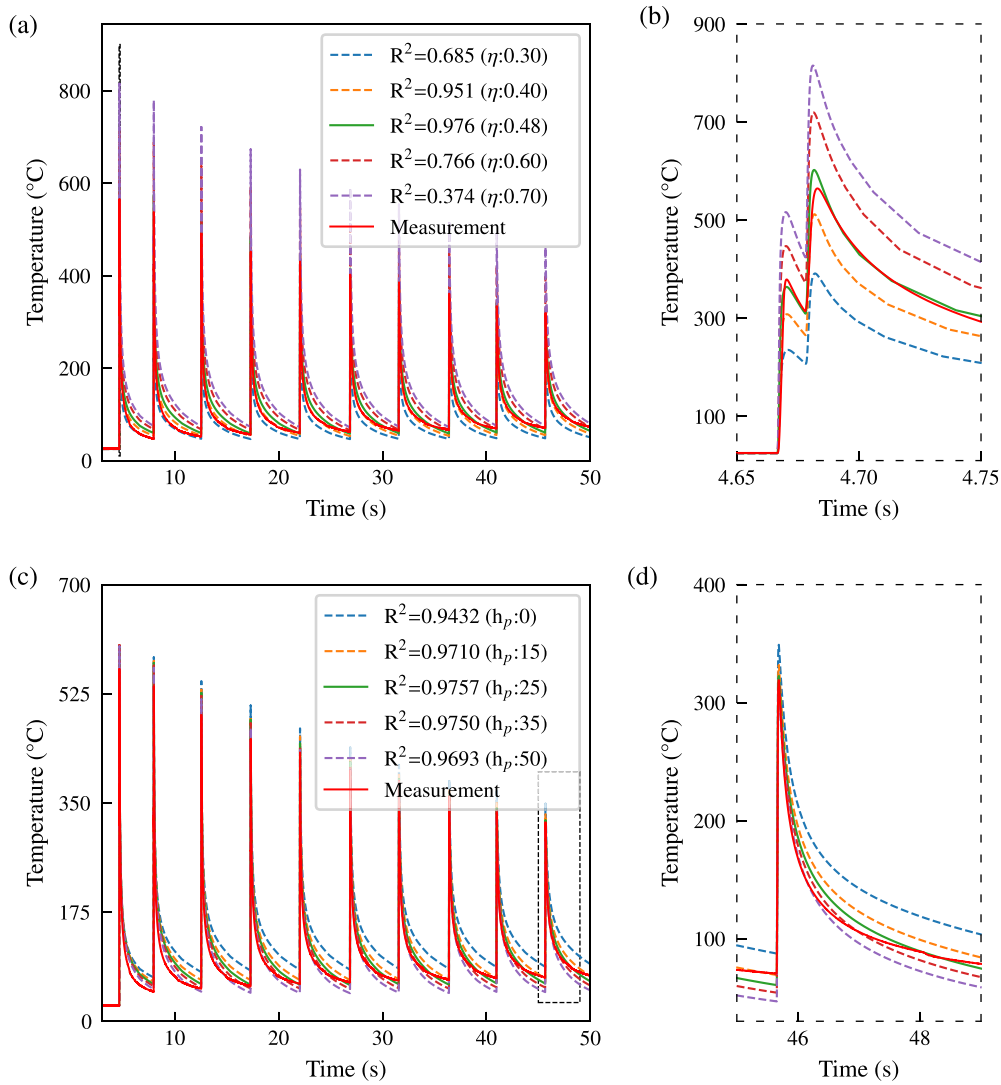
Fig. D.1. Effect of changes in laser absorption coefficient η and equivalent convective powder-bed heat loss factor h_p on simulated temperature histories. (a) Variations in η shift the entire temperature profiles, and more notably the peak temperatures as shown in (b), which zooms on the first layer. (c) Changing h_p has a noticeable effect on the cooling portion of the curves, as further highlighted in (d), which focuses on the 10th deposited layer.

models could significantly reduce the computational cost for reaching mesh-independent results.

CRediT authorship contribution statement

Pooriya Gh Ghanbari: Conceptualization, Methodology, Software, Validation, Formal analysis, Investigation, Writing – original draft, Visualization. **Rafal Wrobel:** Methodology, Investigation, Writing – review & editing. **Bastian Rheingans:** Methodology, Validation, Formal analysis, Investigation, Writing – review & editing. **Thomas Mayer:** Methodology, Validation, Formal analysis, Investigation, Writing – review & editing. **Christian Leinenbach:** Resources, Writing – review & editing. **Edoardo Mazza:** Conceptualization, Resources, Writing – review & editing, Supervision. **Ehsan Hosseini:** Conceptualization, Resources, Writing – review & editing, Supervision, Funding acquisition.

Declaration of competing interest

The authors declare that there is no conflict of interest regarding the publication of the article.

Data availability

The input files to reproduce the FE simulations are available under https://github.com/HighTempIntegrity/Ghanbari_Multiscale2023, and further information will be made available upon request.

Appendix A. Time response of the thermocouples

In measuring highly dynamic temperature changes using thermocouples with a high sampling frequency, a delay with respect to the true temperature is expected due to the time needed for heating up the junction. In this study, thin K-type thermocouple wires with a diameter of 130 μm were used to reduce this effect. To estimate the time-constant

of the measurement set-up, different time-constants $\tau \in (0, 1, 2)$ ms were assumed and the equivalent delayed temperature changes from the FE simulation were calculated as shown in Fig. A.1. Similar to other studies where thin-wire thermocouple pairs were attached to the measurement surface, the time-constant is estimated to be on the order of magnitude of a few milliseconds [75,76]. However, the time lag in thermocouple response was not taken into consideration in this study for comparison of temperature histories from simulations and measurements for simplicity.

Appendix B. Sensitivity analysis

A $2.2 \times 2 \times 0.2$ mm^3 assembly (Fig. B.1(a)) similar to the examined thin-walls in this study, was used to investigate the influence of solidification range and mesh size on the predicted temperature field. In Fig. B.1(b), the temperature profiles over the laser scan path (red line in Fig. B.1(a)) are shown for difference values for the solidification range from 42 °C to 400 °C. Increasing this parameter results in smoother temperature profiles (lower gradients) around the melting point as the latent heat is released over a wider temperature range, but the values remain unaffected at other temperature levels. In Figs. B.1(c) and B.1(d) the model was solved with various mesh refinements using the proposed material model in Section 4, and the constant properties of Section 5, respectively. In both cases the results quickly converge for elements below 50^3 µm^3 in the far-field. For reaching mesh independency in the near-field, 10^3 µm^3 elements are required as shown in Fig. B.1(e). In Fig. B.1(f), the thermal conductivity of the powder layer is reduced to 2% of the solid state and compared with the fully solid scenario. The reduction in heat dissipation with powder has minor impact on the developed temperatures.

Appendix C. Adaptive time incrementation

In FE thermal analysis of the PBF-LB/M process, small time increments are required to capture the transient and steep temperature gradients in the process zone. However, since the validation of the simulation framework was based on *in-situ* temperature measurements at a single location, applying fine incrementation was only needed when the laser was near the thermocouples and larger increments could be used elsewhere. To control time increment size in Abaqus the USDFLD subroutine was used. A Fortran subroutine assessed the distance of the laser centre with respect to the thermocouple location and defined a maximum allowed time increment based on the following equation:

$$\Delta t_{limit} = [(\frac{x_{rel}}{a})^2 + (\frac{y_{rel}}{b})^2 + (\frac{z_{rel}}{c})^2] \times (\Delta t_{max} - \Delta t_{min}) + \Delta t_{min} \quad (C.1)$$

where $a = 5$ mm, $b = 1$ mm, $c = 1$ mm determine the size of an ellipsoid centred on the probe point. The upper limit of time increment at the boundary of the ellipsoid was set to $\Delta t_{max} = 2$ ms with a linear decrease towards the centre reaching a minimum value of $\Delta t_{max} = 0.05$ ms. At each solution increment, when size of the current time increment was smaller than the above limit, the ratio $\Delta t_{limit}/\Delta t_{current}$ was assigned to the PNEWDT parameter to reduce the increment size. It should be noted that this approach does not compromise the convergence criteria in Abaqus standard/implicit. If convergence is not reached, a smaller time increment is applied automatically.

Appendix D. Calibration sensitivity

For finding the best fit between the calculated temperature history and the measured data from the thermocouples, simulations using various combinations of η and h_p were conducted. Fig. D.1, shows the high sensitivity with respect to the laser absorption coefficient, specifically in peak temperature as demonstrated in Fig. D.1. However, in case of h_p the changes in peak temperatures are relatively small as seen in Fig. D.1. Nevertheless, the cooling portion of the curves changes noticeably as shown in Fig. D.1.

References

[1] DebRoy T, Wei HL, Zuback JS, Mukherjee T, Elmer JW, Milewski JO, Beese AM, Wilson-Heid A, De A, Zhang W. Additive manufacturing of metallic components – Process, structure and properties. Prog Mater Sci 2018;92:112–224. http://dx.doi.org/10.1016/j.pmatsci.2017.10.001.

[2] Vafadar A, Guzzomi F, Rassau A, Hayward K. Advances in metal additive manufacturing: A review of common processes, industrial applications, and current challenges. Appl Sci 2021;11(3):1213. http://dx.doi.org/10.3390/app11031213.

[3] Shaji Karapuzha A, Fraser D, Schliephake D, Dietrich S, Zhu Y, Wu X, Huang A. Microstructure, mechanical behaviour and strengthening mechanisms in Hastelloy X manufactured by electron beam and laser beam powder bed fusion. J Alloys Compd 2021;862:158034. http://dx.doi.org/10.1016/j.jallcom.2020.158034.

[4] King WE, Anderson AT, Ferencz RM, Hodge NE, Kamath C, Khairallah SA, Rubenchik AM. Laser powder bed fusion additive manufacturing of metals; physics, computational, and materials challenges. Appl Phys Rev 2015;2(4):041304. http://dx.doi.org/10.1063/1.4937809.

[5] Mower TM, Long MJ. Mechanical behavior of additive manufactured, powder-bed laser-fused materials. Mater Sci Eng A 2016;651:198–213.

[6] Hosseini E, Popovich VA. A review of mechanical properties of additively manufactured Inconel 718. Addit Manuf 2019;30:100877. http://dx.doi.org/10.1016/j.addma.2019.100877.

[7] Tan Z, Gao S, Lan L, He B. Effect of rescanning strategy on residual stress and distortion of two alloys manufactured by selective laser melting. J Mater Eng Perform 2021. http://dx.doi.org/10.1007/s11665-021-05872-4.

[8] Fang Z-C, Wu Z-L, Huang C-G, Wu C-W. Review on residual stress in selective laser melting additive manufacturing of alloy parts. Opt Laser Technol 2020;129:106283. http://dx.doi.org/10.1016/j.optlastec.2020.106283.

[9] Giganto S, Martínez-Pellitero S, Cuesta E, Zapico P, Barreiro J. Proposal of design rules for improving the accuracy of selective laser melting (SLM) manufacturing using benchmarks parts. Rapid Prototyp J 2022;28(6):1129–43. http://dx.doi.org/10.1108/RPJ-06-2021-0130.

[10] Oliveira JP, LaLonde AD, Ma J. Processing parameters in laser powder bed fusion metal additive manufacturing. Mater Des 2020;193:108762. http://dx.doi.org/10.1016/j.matdes.2020.108762.

[11] Spears TG, Gold SA. In-process sensing in selective laser melting (SLM) additive manufacturing. Integr Mater Manuf Innov 2016;5(1):16–40. http://dx.doi.org/10.1186/s40192-016-0045-4.

[12] Chowdhury S, Yadaiah N, Prakash C, Ramakrishna S, Dixit S, Gupta LR, Buddhi D. Laser powder bed fusion: A state-of-the-art review of the technology, materials, properties & defects, and numerical modelling. J Mater Res Technol 2022;20:2109–72. http://dx.doi.org/10.1016/j.jmrt.2022.07.121.

[13] Gatsos T, Elsayed KA, Zhai Y, Lados DA. Review on computational modeling of process–microstructure–property relationships in metal additive manufacturing. JOM 2020;72(1):403–19. http://dx.doi.org/10.1007/s11837-019-03913-x.

[14] Wei HL, Mukherjee T, Zhang W, Zuback JS, Knapp GL, De A, DebRoy T. Mechanistic models for additive manufacturing of metallic components. Prog Mater Sci 2021;116:100703. http://dx.doi.org/10.1016/j.pmatsci.2020.100703.

[15] Fu CH, Guo YB. Three-dimensional temperature gradient mechanism in selective laser melting of Ti-6Al-4V. J Manuf Sci Eng 2014;136(6). http://dx.doi.org/10.1115/1.4028539.

[16] Keshavarzkermani A, Marzbanrad E, Esmaeilizadeh R, Mahmoodkhani Y, Ali U, Enrique PD, Zhou NY, Bonakdar A, Toyserkani E. An investigation into the effect of process parameters on melt pool geometry, cell spacing, and grain refinement during laser powder bed fusion. Opt Laser Technol 2019;116:83–91. http://dx.doi.org/10.1016/j.optlastec.2019.03.012.

[17] Rafi HK, Karthik NV, Gong H, Starr TL, Stucker BE. Microstructures and mechanical properties of Ti6Al4V parts fabricated by selective laser melting and electron beam melting. J Mater Eng Perform 2013;22(12):3872–83. http://dx.doi.org/10.1007/s11665-013-0658-0.

[18] Harrison NJ, Todd I, Mumtaz K. Reduction of micro-cracking in nickel superalloys processed by Selective Laser Melting: A fundamental alloy design approach. Acta Mater 2015;94:59–68. http://dx.doi.org/10.1016/j.actamat.2015.04.035.

[19] Mercelis P, Kruth J-P. Residual stresses in selective laser sintering and selective laser melting. Rapid Prototyp J 2006;12(5):254–65. http://dx.doi.org/10.1108/13552540610707013.

[20] Wang F. Mechanical property study on rapid additive layer manufacture Hastelloy® X alloy by selective laser melting technology. Int J Adv Manuf Technol 2012;58(5):545–51. http://dx.doi.org/10.1007/s00170-011-3423-2.

[21] Ren C-G, Lo Y-L, Tran H-C, Lee M-H. Emissivity calibration method for pyrometer measurement of melting pool temperature in selective laser melting of stainless steel 316L. Int J Adv Manuf Technol 2019;105(1):637–49. http://dx.doi.org/10.1007/s00170-019-04193-0.

[22] Bayle F, Doubenskaia M. Selective laser melting process monitoring with high speed infra-red camera and pyrometer. In: Fundamentals of laser assisted micro- and nanotechnologies, Vol. 6985. International Society for Optics and Photonics; 2008, 698505. http://dx.doi.org/10.1117/12.786940.

[23] Yadroitsev I, Krakhmalev P, Yadroitsava I. Selective laser melting of Ti6Al4V alloy for biomedical applications: Temperature monitoring and microstructural evolution. J Alloys Compd 2014;583:404–9. http://dx.doi.org/10.1016/j.jallcom.2013.08.183.

[24] Hooper PA. Melt pool temperature and cooling rates in laser powder bed fusion. Addit Manuf 2018;22:548–59. http://dx.doi.org/10.1016/j.addma.2018.05.032.

[25] Mohr G, Nowakowski S, Altenburg SJ, Maierhofer C, Hilgenberg K. Experimental determination of the emissivity of powder layers and bulk material in laser powder bed fusion using infrared thermography and thermocouples. Metals 2020;10(11):1546. http://dx.doi.org/10.3390/met10111546.

[26] Lane B, Moylan S, Whitenton EP, Ma L. Thermographic measurements of the commercial laser powder bed fusion process at NIST. Rapid Prototyp J 2016;22(5):778–87. http://dx.doi.org/10.1108/RPJ-11-2015-0161.

[27] Dunbar AJ, Denlinger ER, Heigel J, Michaleris P, Guerrier P, Martukanitz R, Simpson TW. Development of experimental method for in situ distortion and temperature measurements during the laser powder bed fusion additive manufacturing process. Addit Manuf 2016;12:25–30. http://dx.doi.org/10.1016/j.addma.2016.04.007.

[28] Denlinger ER, Jagdale V, Srinivasan GV, El-Wardany T, Michaleris P. Thermal modeling of Inconel 718 processed with powder bed fusion and experimental validation using in situ measurements. Addit Manuf 2016;11:7–15. http://dx.doi.org/10.1016/j.addma.2016.03.003.

[29] Denlinger ER, Gouge M, Irwin J, Michaleris P. Thermomechanical model development and in situ experimental validation of the Laser Powder-Bed Fusion process. Addit Manuf 2017;16:73–80. http://dx.doi.org/10.1016/j.addma.2017.05.001.

[30] Luo Z, Zhao Y. Efficient thermal finite element modeling of selective laser melting of Inconel 718. Comput Mech 2020;65(3):763–87. http://dx.doi.org/10.1007/s00466-019-01794-0.

[31] Zhang Q, Xie J, Gao Z, London T, Griffiths D, Oancea V. A metallurgical phase transformation framework applied to SLM additive manufacturing processes. Mater Des 2019;166:107618. http://dx.doi.org/10.1016/j.matdes.2019.107618.

[32] Chiumenti M, Neiva E, Salsi E, Cervera M, Badia S, Moya J, Chen Z, Lee C, Davies C. Numerical modelling and experimental validation in Selective Laser Melting. Addit Manuf 2017;18:171–85. http://dx.doi.org/10.1016/j.addma.2017.09.002.

[33] An N, Yang G, Yang K, Wang J, Li M, Zhou J. Implementation of Abaqus user subroutines and plugin for thermal analysis of powder-bed electron-beam-melting additive manufacturing process. Mater Today Commun 2021;27:102307. http://dx.doi.org/10.1016/j.mtcomm.2021.102307.

[34] Song X, Feih S, Zhai W, Sun C-N, Li F, Maiti R, Wei J, Yang Y, Oancea V, Romano Brandt L, Korsunsky AM. Advances in additive manufacturing process simulation: Residual stresses and distortion predictions in complex metallic components. Mater Des 2020;193:108779. http://dx.doi.org/10.1016/j.matdes.2020.108779.

[35] Li Y, Zhou K, Tan P, Tor SB, Chua CK, Leong KF. Modeling temperature and residual stress fields in selective laser melting. Int J Mech Sci 2018;136:24–35. http://dx.doi.org/10.1016/j.ijmecsci.2017.12.001.

[36] Moser D, Cullinan M, Murthy J. Multi-scale computational modeling of residual stress in selective laser melting with uncertainty quantification. Addit Manuf 2019;29:100770. http://dx.doi.org/10.1016/j.addma.2019.06.021.

[37] Chernyshikhin SV, Firsov DG, Shishkovsky IV. Selective laser melting of pre-alloyed NiTi powder: Single-track study and FE modeling with heat source calibration. Materials 2021;14(23):7486. http://dx.doi.org/10.3390/ma14237486.

[38] Liu M, Chiu LNS, Vundru C, Liu Y, Huang A, Davies C, Wu X, Yan W. A characteristic time-based heat input model for simulating selective laser melting. Addit Manuf 2021;44:102026. http://dx.doi.org/10.1016/j.addma.2021.102026.

[39] Hocine S, Van Swygenhoven H, Van Petegem S. Verification of selective laser melting heat source models with operando X-ray diffraction data. Addit Manuf 2021;37:101747. http://dx.doi.org/10.1016/j.addma.2020.101747.

[40] Cook PS, Murphy AB. Simulation of melt pool behaviour during additive manufacturing: Underlying physics and progress. Addit Manuf 2020;31:100909. http://dx.doi.org/10.1016/j.addma.2019.100909.

[41] Wei HL, Mukherjee T, Zhang W, Zuback JS, Knapp GL, De A, DebRoy T. Mechanistic models for additive manufacturing of metallic components. Prog Mater Sci 2020;100703. http://dx.doi.org/10.1016/j.pmatsci.2020.100703.

[42] Ren Z, Wei D, Wang S, Zhang DZ, Mao S. On the role of pre- and post-contour scanning in laser powder bed fusion: Thermal-fluid dynamics and laser reflections. Int J Mech Sci 2022;226:107389. http://dx.doi.org/10.1016/j.ijmecsci.2022.107389.

[43] Zaeh MF, Branner G. Investigations on residual stresses and deformations in selective laser melting. Prod Eng 2010;4:35–45. http://dx.doi.org/10.1007/s11740-009-0192-y.

[44] Neiva E, Chiumenti M, Cervera M, Salsi E, Piscopo G, Badia S, Martín AF, Chen Z, Lee C, Davies C. Numerical modelling of heat transfer and experimental validation in powder-bed fusion with the virtual domain approximation. Finite Elem Anal Des 2020;168:103343. http://dx.doi.org/10.1016/j.finel.2019.103343.

[45] Parry L, Ashcroft IA, Wildman RD. Understanding the effect of laser scan strategy on residual stress in selective laser melting through thermo-mechanical simulation. Addit Manuf 2016;12:1–15. http://dx.doi.org/10.1016/j.addma.2016.05.014.

[46] Lu Y, Wu S, Gan Y, Huang T, Yang C, Junjie L, Lin J. Study on the microstructure, mechanical property and residual stress of SLM Inconel-718 alloy manufactured by differing island scanning strategy. Opt Laser Technol 2015;75:197–206. http://dx.doi.org/10.1016/j.optlastec.2015.07.009.

[47] Song J, Wu W, Zhang L, He B, Lu L, Ni X, Long Q, Zhu G. Role of scanning strategy on residual stress distribution in Ti-6Al-4V alloy prepared by selective laser melting. Optik 2018;170:342–52. http://dx.doi.org/10.1016/j.ijleo.2018.05.128.

[48] Zinovieva O, Romanova V, Zinoviev A, Nekhorosheva O, Balokhonov R. Elastic properties of additively manufactured steel produced with different scan strategies. Int J Mech Sci 2023;244:108089. http://dx.doi.org/10.1016/j.ijmecsci.2022.108089.

[49] Pal D, Patil N, Zeng K, Teng C, Stucker B. An efficient multi-scale simulation architecture for the prediction of performance metrics of parts fabricated using additive manufacturing. Metall Mater Trans A 2015;46(9):3852–63. http://dx.doi.org/10.1007/s11661-015-2903-7.

[50] Patil N, Pal D, Khalid Rafi H, Zeng K, Moreland A, Hicks A, Beeler D, Stucker B. A generalized feed forward dynamic adaptive mesh refinement and derefinement finite element framework for metal laser sintering—Part I: Formulation and algorithm development. J Manuf Sci Eng 2015;137(4):041001–041001–15. http://dx.doi.org/10.1115/1.4030059.

[51] Pitassi D, Savoia E, Fontanari V, Molinari A, Luchin V, Zappini G, Benedetti M. Finite element thermal analysis of metal parts additively manufactured via selective laser melting. In: Păcurar R, editor. Finite element method - Simulation, numerical analysis and solution techniques. Rijeka: IntechOpen; 2017, http://dx.doi.org/10.5772/intechopen.71876, Ch. 6.

[52] Khan K, De A. Modelling of selective laser melting process with adaptive remeshing. Sci Technol Weld Join 2019;24(5):391–400. http://dx.doi.org/10.1080/13621718.2019.1575057.

[53] Olleak A, Xi Z. Part-scale finite element modeling of the selective laser melting process with layer-wise adaptive remeshing for thermal history and porosity prediction. J Manuf Sci Eng 2020;142(12). http://dx.doi.org/10.1115/1.4047733.

[54] Foteinopoulos P, Papacharalampopoulos A, Stavropoulos P. On thermal modeling of Additive Manufacturing processes. CIRP J Manuf Sci Technol 2018;20:66–83. http://dx.doi.org/10.1016/j.cirpj.2017.09.007.

[55] Gh Ghanbari P, Mazza E, Hosseini E. Adaptive local-global multiscale approach for thermal simulation of the selective laser melting process. Addit Manuf 2020;101518. http://dx.doi.org/10.1016/j.addma.2020.101518.

[56] Tascioglu E, Karabulut Y, Kaynak Y. Influence of heat treatment temperature on the microstructural, mechanical, and wear behavior of 316L stainless steel fabricated by laser powder bed additive manufacturing. Int J Adv Manuf Technol 2020;107(5):1947–56. http://dx.doi.org/10.1007/s00170-020-04972-0.

[57] Salikhyanov D, Veselova V, Volkov V. Flow behavior and microstructure evolution of Ti-6Al-4V titanium alloy produced by selective laser melting compared to wrought. Int J Adv Manuf Technol 2021. http://dx.doi.org/10.1007/s00170-021-08000-7.

[58] Mills KC. Recommended values of thermophysical properties for selected commercial alloys. Woodhead Publishing; 2002.

[59] Hastelloy X - Haynes International. 2021, https://www.haynesintl.com/alloys/alloy-portfolio_/High-temperature-Alloys/HASTELLOY-X-alloy, accessed: 2021-08-24.

[60] Ulan kyzy S, Völkl R, Munz O, Fischer T, Welzenbach S, Glatzel U. Thermophysical properties of Hastelloy X and Haynes 214 close to the melting range. Mater Sci Technol 2020;36(10):1012–9. http://dx.doi.org/10.1080/02670836.2020.1753154.

[61] Takeda T, Kunitomi K, Horie T, Iwata K. Feasibility study on the applicability of a diffusion-welded compact intermediate heat exchanger to next-generation high temperature gas-cooled reactor. Nucl Eng Des 1997;168(1):11–21. http://dx.doi.org/10.1016/S0029-5493(96)01361-1.

[62] Clark III LM, Taylor RE. Radiation loss in the flash method for thermal diffusivity. J Appl Phys 1975;46(2):714–9. http://dx.doi.org/10.1063/1.321635.

[63] Cape JA, Lehman GW. Temperature and finite pulse-time effects in the flash method for measuring thermal diffusivity. J Appl Phys 1963;34(7):1909–13. http://dx.doi.org/10.1063/1.1729711.

[64] Opfermann JD, Blumm J. Vorrichtung zur bestimmung der wärmeleitfähigkeit mittels lichpulsen. 2005.

[65] Kim S, Kuk IH, Kim JS. Order–disorder reaction in Alloy 600. Mater Sci Eng A 2000;279(1):142–8. http://dx.doi.org/10.1016/S0921-5093(99)00640-1.

[66] Gan Z, Lian Y, Lin SE, Jones KK, Liu WK, Wagner GJ. Benchmark study of thermal behavior, surface topography, and dendritic microstructure in selective laser melting of Inconel 625. Integr Mater Manuf Innov 2019;8(2):178–93. http://dx.doi.org/10.1007/s40192-019-00130-x.

[67] Proell SD, Wall WA, Meier C. On phase change and latent heat models in metal additive manufacturing process simulation. Adv Model Simul Eng Sci 2020;7(1):24. http://dx.doi.org/10.1186/s40323-020-00158-1.

[68] Goldak J, Chakravarti A, Bibby M. A new finite element model for welding heat sources. Metall Trans B 1984;15(2):299–305. http://dx.doi.org/10.1007/BF02667333.

[69] Li C, Gouge MF, Denlinger ER, Irwin JE, Michaleris P. Estimation of part-to-powder heat losses as surface convection in laser powder bed fusion. Addit Manuf 2019;26:258–69. http://dx.doi.org/10.1016/j.addma.2019.02.006.

[70] Shahabad SI, Zhang Z, Keshavarzkermani A, Ali U, Mahmoodkhani Y, Esmaeilizadeh R, Bonakdar A, Toyserkani E. Heat source model calibration for thermal analysis of laser powder-bed fusion. Int J Adv Manuf Technol 2020;106(7):3367–79. http://dx.doi.org/10.1007/s00170-019-04908-3.

[71] Trapp J, Rubenchik AM, Guss G, Matthews MJ. In situ absorptivity measurements of metallic powders during laser powder-bed fusion additive manufacturing. Appl Mater Today 2017;9:341–9. http://dx.doi.org/10.1016/j.apmt.2017.08.006.

[72] Song J, Zhang L, Wu W, He B, Ni X, Xu J, Zhu G, Yang Q, Wang T, Lu L. Understanding processing parameters affecting residual stress in selective laser melting of Inconel 718 through numerical modeling. J Mater Res 2019;34(8):1395–404. http://dx.doi.org/10.1557/jmr.2018.504.

[73] Xie J, Oancea V, Hurtado J. Phase transformations in metals during additive manufacturing processes. In: NAFEMS world congress. 2017.

[74] Hosseini E, Ghanbari PG, Keller F, Marelli S, Mazza E. Deploying artificial intelligence for component-scale multi-physical field simulation of metal additive manufacturing. In: Meboldt M, Klahn C, editors. Industrializing additive manufacturing. Cham: Springer International Publishing; 2021, p. 268–76. http://dx.doi.org/10.1007/978-3-030-54334-1_19.

[75] Alcini WV. Experimental measurement of liquid nugget heat convection in spot welding. Weld J 1990;69(5):177s–80s.

[76] Schmale J, Fehrenbacher A, Shrivastava A, Pfefferkorn FE. Calibration of dynamic tool–workpiece interface temperature measurement during friction stir welding. Measurement 2016;88:331–42. http://dx.doi.org/10.1016/j.measurement.2016.02.065.